

Efficient Mineralization of Toluene by W-Doped TiO₂ Nanofibers Under Visible Light Irradiation

Li Zhang¹, Yaogang Li², Hongyong Xie³, Hongzhi Wang^{1,*}, and Qinghong Zhang^{2,*}

¹State Key Laboratory for Modification of Chemical Fibers and Polymer Materials,
College of Materials Science and Engineering, Donghua University,
Shanghai 201620, China

²Engineering Research Center of Advanced Glasses Manufacturing Technology, MOE,
College of Materials Science and Engineering, Donghua University,
Shanghai 201620, China

³School of Urban Development and Environmental Engineering, Shanghai Second Polytechnic University,
Shanghai 201209, China

Toxic toluene gas caused enormous harm to human health, and the traditional method to deal with this puzzle is using physical adsorption, which just transfer the toluene from one medium to another. Photocatalysis has great potential to mineralize toluene into CO₂ under visible light irradiation, but their applications have been limited by difficulties in preparing efficient photocatalysts with fine crystallite size, considerable visible light response, and large surface area to contact with toluene gas. To address this problem, we have developed a film composed of W-doped TiO₂ nanofibers to mineralize toluene under visible light irradiation. The electrospinning preparation route allows incorporation of up to 50 wt% of W in substitutional positions of titanium atom in the anatase network. The W-doped TiO₂ nanofibers behave finer crystallite size, stronger visible light absorbance, and larger surface area comparing with pure TiO₂ nanofibers. The nanofiber structured morphology on the quartz tube promotes the reaction rates for the gas-phase photo-oxidation of toluene. The concentrations of the produced CO₂ keep steady during the photodegradation process, indicating the practicality and operability for the whole experiment. This research is conducive to the development of novel photocatalytic materials to efficiently mineralize toxic gas pollutants including toluene for practical application.

Keywords: Photocatalyst, Visible Light Photocatalysis, Nanofibers, Toluene, TiO₂.

1. INTRODUCTION

Toluene is a common organic solvent which is widely used in both industrial and domestic activities, such as in preparing aviation gasoline,¹ dyes,² adhesives,³ and paints.⁴ Repeatedly breathing air contaminated by toluene over long periods of time can cause death, permanent brain damage, or depression.⁵ Accordingly, there is a growing interest in developing good air purification methods for the removal of volatile toluene from indoor air. Physical adsorption, using charcoal or activated carbon, has been investigated to remove the toluene, but this method just transfer the toluene from one medium to another.⁶ Consequently, it is crucial to develop environmentally benign routes combining effective adsorption

with enhanced photocatalytic efficiency, which completely mineralizes the organic pollutants.

Photocatalytic oxidation that mostly using titania (TiO₂) based materials as the catalyst has attracted substantial attention in recent years, as it is cost-effective, high catalytic stability and can be carried out at room temperature and atmospheric pressure.^{7,8} However, its practical application has been limited because of its large energy band gap (3.2 eV) that requires UV light to excite the photocatalytic reactions.⁹ In view of better utilization of solar light, in nowadays, doping with other elements in TiO₂ has drawn a great deal of attentions to extend the spectral response from the UV range into the visible region. For instance, Asahi et al. found that N doped TiO₂ was visible light active due to the interaction of N2p and O2p orbitals, which can lead to the up-shifting of TiO₂ valence band.¹⁰

*Authors to whom correspondence should be addressed.

Xie et al. have synthesized C doped TiO₂ nanoparticles and studied their photocatalytic activity on toluene.¹¹ Fuente et al. have explored the doping of the anatase structure using high concentrations of nine different dopants and showed that W was one of the best options for toluene photodegradation using sunlight-type excitation.¹² W doping anatase structure appears to potentially affect photoactivity by three different factors, namely the increasing visible light response, the presence of surface W centers enhancing oxygen activation, and finally, the creation of new surface centers with modified interaction with toluene.¹³ In these studies, though anionic or cationic doping TiO₂ systems showed good photocatalytic properties, they are usually in the form of agglomerated particles, so the gas molecules had a relative low rate to diffuse into the interior parts. Thin porous films composed of nanofibers provide a new way to solve this problem. Compared with nanoparticles, nanofibers have more advantages on photodegradation of volatile toluene, because they take advantage of special characteristics such as large surface area-to-volume ratio, 3 dimensional (3-D) open structure and ease of fabrication.^{14,15} However, to the best of our knowledge, there was no report on efficient mineralization of toluene using porous films composed of W-doped TiO₂ nanofibers under visible light irradiation.

In this work, we prepared porous films composed of W-doped TiO₂ nanofibers with different doping concentrations and studied the influence of W-doping level on the photomineralization of toluene. The nanofibers were prepared by electrospinning method allowing doping of up to ca. 50 wt% of W in substitutional positions of the anatase structure. The influences of the crystallite size, the crystallographic phases, the surface area, and the chemical states on the activity of the photocatalysts were also discussed.

2. EXPERIMENTAL DETAILS

2.1. Sample Preparation

The TiO₂ nanofibers were typically prepared by electrospinning a solution containing 4.0 g tetrabutyl titanate (Ti(OC₄H₉)₄, Shanghai Chemical Reagent Company) mixed with tungsten hexachloride (WCl₆, 99.99%, Aldrich), 4.0 mL acetic acid (glacial, Shanghai Chemical Reagent Company), 1.4 g poly(vinyl pyrrolidone) (PVP) ($M_w \approx 1.3 \times 10^6$, Aldrich) and 13 mL ethanol. The solution was ultrasonicated for 2 h to ensure the homogeneity

followed by loading into a 10 mL plastic syringe with a 21 gauge stainless steel needle at the tip. The needle was electrified by a 13 kV high-voltage DC supply. The solution was pumped continuously by a syringe pump (Model 22, Harvard Apparatus, USA) with a rate of 2.5 mL/h. A grounded wire netting was used as electrode to collect the nanofibers. The as-spun fibers were calcined at 500 °C for 2 h to burn out the organic compounds and obtain inorganic W-doped TiO₂ fibers. Five samples of W-doped TiO₂ nanofibers with different W weight percentage were fabricated, and were denoted as TW0, TW10, TW20, TW30 and TW50, respectively (see Table I). The digits represent the W/(W + Ti) ratio in weight.

2.2. Sample Characterization

The morphology of the samples were characterized with a field emission scanning electron microscope (FESEM, Hitachi S-4800) operated at an accelerating voltage of 20 kV. TEM images were obtained using a JEM-2100 F TEM (JEOL Tokyo Japan) operating at 200 kV equipped with a LINK probe for energy dispersive X-ray (EDX) spectroscopy analysis. X-ray diffraction (XRD) was carried out on a Rigaku-D/max 2550 PC (Japan) diffractometer with Cu K α radiation ($\lambda = 1.5406 \text{ \AA}$). X-ray photoelectron spectroscopy (XPS) measurements were carried out with an SECA Lab 220i-XL spectrometer by using an unmonochromated Al K α (1486.6 eV) X-ray source. All the spectra were calibrated to the binding energy of the adventitious C 1s peak at 284.6 eV. The porous properties of samples were investigated using physical adsorption of N₂ at liquid-nitrogen temperature on an automatic volumetric sorption analyzer Autosorb-1 MP (Quantachrom SI, USA). UV-vis diffuse reflectance spectroscopy (DRS) spectra were recorded on a PE Lambda 950 instrument, using BaSO₄ as the reference sample.

2.3. Photoreactivity Measurements

The experimental set-up and photoreactor used for gas phase photo-oxidation of toluene is designed according the method previously reported.¹¹ The photoreactor was made of a quartz tube, a fluorescent lamp and light shield. The quartz tube had an inner diameter of 80 mm, and an effective length of 1200 mm. The catalyst was painted onto the inner wall of the quartz tube from a concentrated suspension of the TiO₂ nanofibers. After a day of ambient drying,

Table I. W percentage, BET surface area, crystallite size, mean pore diameter, pore volume and mineralization degree of the W-doped TiO₂ nanofibers.

Sample	W percentage (W/(W + Ti), wt%)	Surface area (m ² g ⁻¹)	Crystallite size (nm)	Pore diameter (nm)	Pore volume (cm ³ g ⁻¹)	Mineralization degree (%)
TW0	0	46.0	26.0	6.911	0.153	20.5
TW10	10	61.8	13.9	3.621	0.076	45.8
TW20	20	79.2	10.5	3.578	0.074	76.6
TW30	30	84.5	10.4	3.465	0.059	58.5
TW50	50	104.8	10.2	3.235	0.043	37.4

the catalyst formed a uniform coating that exhibited good adhesion on the quartz support. After three times of the operation, the thickness of thin film composed of TiO₂ nanofibers was ca. 300 nm. A fluorescent lamp (Philips TL-D 36W/54-765), 1200 mm long, was placed in the center of the quartz tube to give 12 mW/cm² fluorescent irradiation with the spectrum in the visible region. The residence time of the air stream in the photoreactor was about 5.7 s with the relative humidity of 80% and initial toluene concentration of 6–300 mg/m³. The air stream was sampled every 30 min at both the inlet and outlet using Tenax tubes at a flow rate of 0.5 L/min for 1–5 min corresponding to the air flow rate via the toluene generator from 0.02 to 0.6 L/min. Reaction rates were evaluated under steady state conditions, typically achieved after 3–4 h from the beginning of irradiation. The toluene in the tube was refilled every 3 h to make the toluene concentration in a constant value. The toluene concentration of the air stream was analyzed by gas chromatography/mass spectrometry (GC/MS, Shimadzu QP2010 plus).

3. RESULTS AND DISCUSSION

SEM images of W-doped TiO₂ nanofibers after calcining at 500 °C for 2 h were shown in Figures 1(a)–(e). All these composite fibers have similar one-dimensional texture structure and are randomly oriented forming non-woven mats. Each sample has a narrow diameter distribution. The diameters of nanofibers decreased from 100 nm to 50 nm with increasing W content in the W-doped TiO₂ from 0 to 20 wt%, while the diameters of TW30 and TW50 are 80 nm and 90 nm. The diameters of TiO₂ and WO₃ nanofibers prepared by electrospinning method were reported to be ca. 200 nm and 100–500 nm, respectively.^{16,17} The results indicate that adding different contents of WCl₆ into the electrospinning solution would change the physical and chemical properties of the spinning solution which has a great impact on the spinning process. In contrast to previous reports about single-component titanium or tungstate salts, the preparations of the W-doped TiO₂ nanofibers started from the sol-gel process of the tetrabutyl titanate and tungsten hexachloride together. The tetrabutyl titanate was hydrolyzed for 2 h and then tungsten hexachloride were added into the system. During the process, Ti—O—Ti, Ti—O—W and W—O—W bonds were formed and stabilized by acetylacetone.¹⁸ The increasing of Ti—O—W bonds in the solution led to a low conductivity fluids, which was beneficial to the formation of thinner nanofibers. However, in the spinning solutions of TW30 and TW50, too much W—O—W bonds were formed thus decreasing the concentration of Ti—O—W bonds, so the diameters of TW30 and TW50 increased compared with TW20. Figure 1(f) shows the digital photo of TW0 and TW50. With increasing W content in the spinning solution, the obtained W-doped nanofibers gradually deepened in color

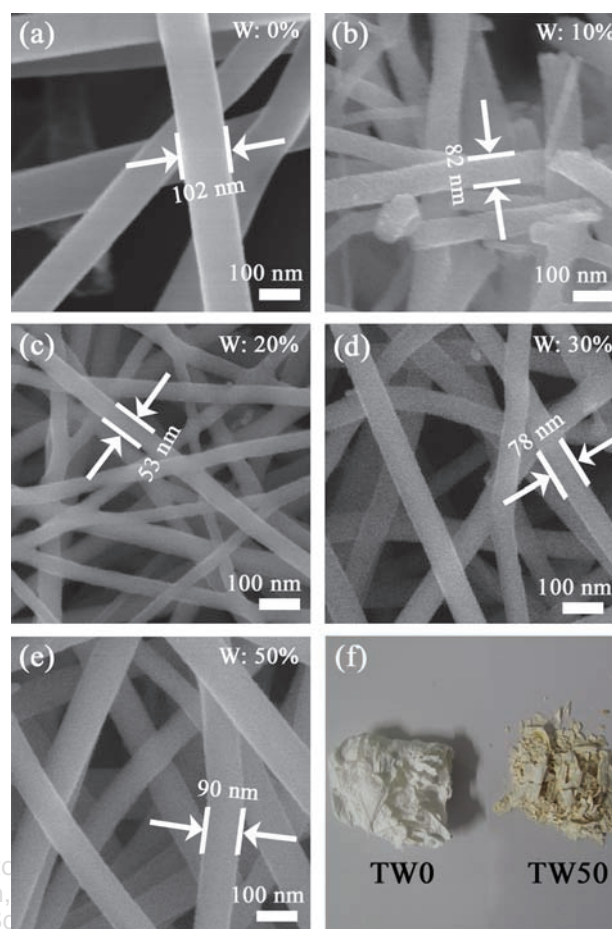


Figure 1. SEM images of (a) TW0, (b) TW10, (c) TW20, (d) TW30, and (e) TW50. (f) Digital photo of TW0 and TW50.

from white (TW0) to pale yellow (TW50), indicating the visible photoactivity of the doped nanofibers. TEM image of TW20 (Fig. 2(a)) confirms the one-dimensional texture structure of the nanofibers with the diameter of 50 nm. The nanofibers are porous, as shown in Figure 2(b) of a single fiber, indicating a large surface area for adsorption of toluene. As expected, the specific surface area and pore volume of TW20 are 79.2 m² g⁻¹ and 0.074 cm³ g⁻¹. As shown in HRTEM image (Fig. 2(c)), TiO₂ nanofibers with the fringe spacing of 0.35 nm corresponding to (1 0 1) facets of anatase are observed.¹⁹ The inset of Figure 2(c) shows the selected area electron diffraction pattern of TW20, and the diffraction rings indicate the polycrystalline nature of the nanofibers.²⁰ A dark-field TEM image with corresponding EDX elemental mapping of the same nanofiber region indicates spatial distribution of O (blue), W (green), and Ti (red), as shown in Figure 2(d).

Figure 3(a) shows the XRD patterns of TW0, TW10, TW20, TW30 and TW50 after calcinations at 500 °C. The diffraction peaks of the W-doped TiO₂ nanofibers can be indexed to (1 0 1), (0 0 4), (2 0 0), (1 0 5), (2 1 1), (2 0 4) and (2 1 5) crystal planes of TiO₂ (JCPDS File No. 21-1272). All the peaks of the W-doped TiO₂ nanofibers can

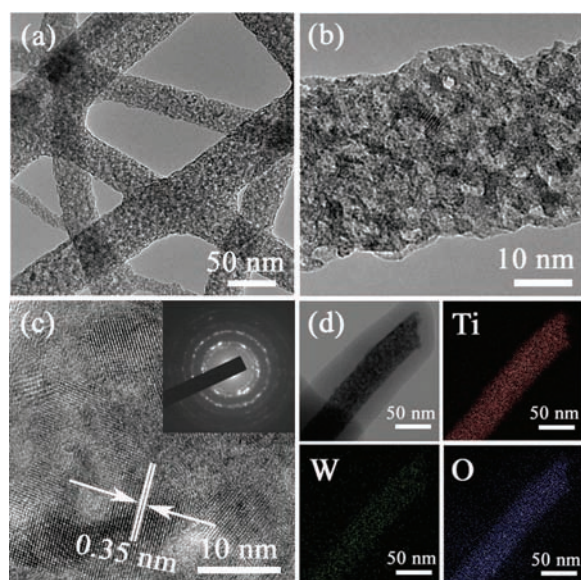


Figure 2. (a) TEM, (b) HR-TEM, (c) HR-TEM with the inset of the SAED patterns, and (d) EDX images of TW20.

be assigned to the anatase phase and no peaks for WO₃ were observed. The crystallite sizes are 15.6, 13.9, 10.5, 10.4 and 10.2 nm for TW0, TW10, TW20, TW30 and TW50, respectively, calculated from X-ray line broadening (ω) according to the Scherrer formula:

$$d = 0.89\lambda / \omega \cos \theta$$

where λ is the X-ray wavelength, 1.5406 Å (CuK α), and θ is the diffraction angle. The intensity of diffraction peaks decreased with increasing W content in the composites, which also suggested that the finer crystallite size of TiO₂ were formed in the presence of W-doping TiO₂ nanofibers. The diffraction peaks of TW20 moved to the right by 0.5 degrees compared with the expected peak positions of the anatase TiO₂ (JCPDS File No. 21-1272), as shown in Figure 3(b). It can be attributed to doping of W⁶⁺ into the TiO₂ crystal lattice, as the effective ionic radii of W⁶⁺ and Ti⁴⁺ are 0.058 nm and 0.061 nm, respectively.²¹

Figure 4 shows the high-resolution Ti 2p and W 4f XPS spectra of TW20. As shown in Figure 4(a), there are two peaks in the Ti 2p region. The peak located at 464.5 eV corresponds to the Ti 2p_{1/2} and another one located at 458.8 eV is assigned to Ti 2p_{3/2}.²² The splitting between Ti 2p_{1/2} and Ti 2p_{3/2} is 5.7 eV, indicating a normal state of Ti⁴⁺ in TW20. In Figure 4(b), the W 4f_{7/2} peak is located at 35.5 eV and the W 4f_{5/2} peak is found at 37.4 eV. The splitting of the 4f doublet of W is 1.9 eV, indicating that the valence state of W doped in TiO₂ nanofibers is +6.²³

The optical absorption property, which is relevant to the electronic structure feature, is considered as a key factor in determining photocatalytic behavior. Figure 5 presents the DRS spectra of the as-prepared samples. Pure TiO₂ nanofibers displayed no obvious absorbance in visible light region due to its large band gap (3.2 eV for

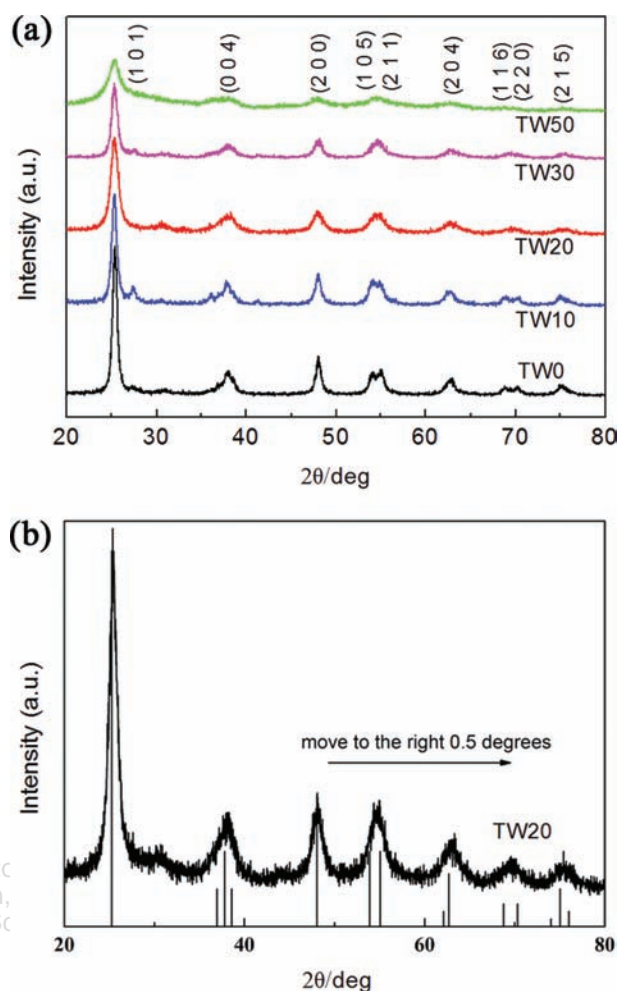


Figure 3. (a) XRD patterns of the W-doped TiO₂ nanofibers. (b) XRD pattern of TW20, with the vertical lines showing the standard peak positions of anatase TiO₂.

anatase, and 3.0 eV for rutile). All W-doped TiO₂ samples exhibited spectral response in the visible region (from 400 to 700 nm), and the absorbance became stronger with increasing of W content from 0 wt% to 50 wt% because of narrower band gap induced by the energy state of W⁶⁺ 5d levels lying below the conduction band of TiO₂.²⁴ In pure anatase, the absorption is associated with the O²⁻-Ti⁴⁺ charge transfer corresponding to electronic excitation from the valence band (O 2p character) to the conduction band (Ti 3d character),²⁵ while in the W-doped TiO₂ samples the presence of donor levels (W⁶⁺ 5d levels) made the conduction band broader, thus decreasing the band gap between the conduction band and the valence band, as shown in Scheme 1.

Figure 6 shows the nitrogen adsorption/desorption isotherm curves of pure TiO₂ and W-doped TiO₂ nanofibers. All the samples show similar type-IV isotherms, indicating the presence of mesopores in the nanofibers.²⁶ The specific surface area of TW0, TW10, TW20, TW30 and TW50 are 46.0, 61.8, 79.2, 84.5 and 104.8 m²/g,

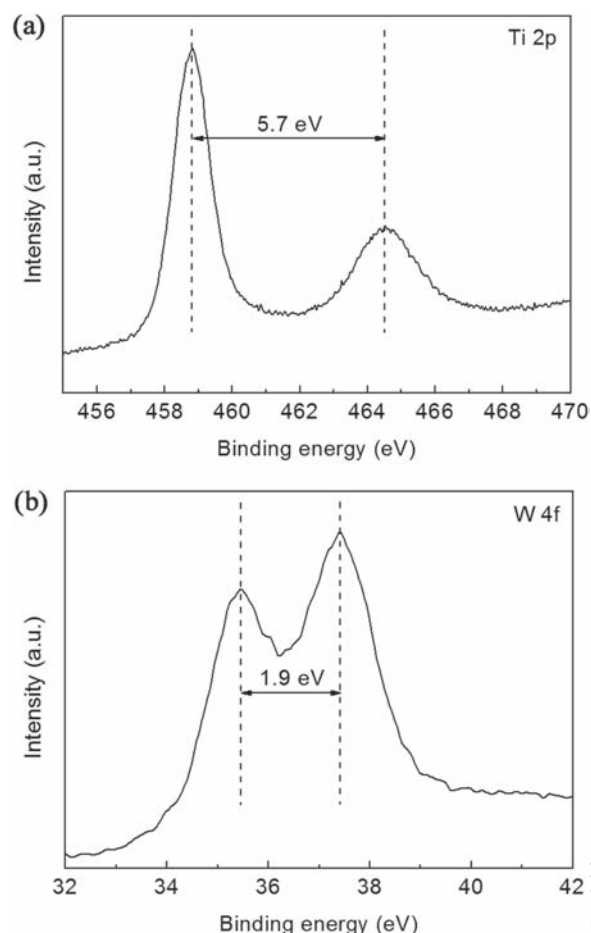


Figure 4. X-ray photoelectron spectroscopy of (a) Ti 2p and (b) W 4f of TW20.

while the pore volumes of the four samples are 0.153, 0.076, 0.074, 0.059 and 0.043 cm³/g, respectively (see Table I). The increased specific surface area and decreased pore volumes of the samples from TW0 to TW50 indicates that with increasing W content in the nanofibers the

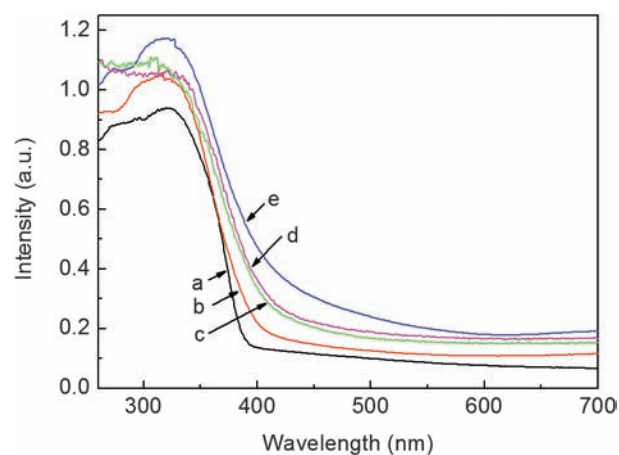
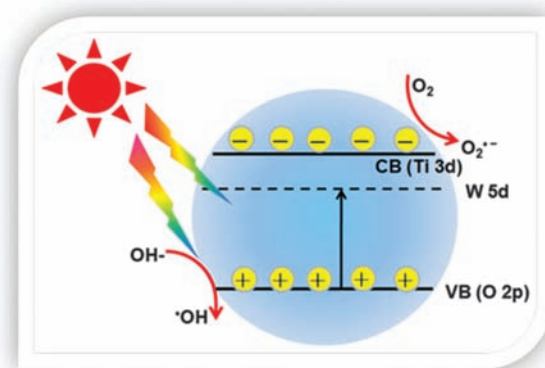


Figure 5. UV-vis diffuse reflectance spectroscopy (DRS) of (a) TW0, (b) TW10, (c) TW20, (d) TW30 and (e) TW50.



Scheme 1. Proposed mechanism of photocatalytic reaction on W-doped TiO₂ photocatalyst.

amount of pores increased even though the pores have smaller sizes. As shown in Figure 6, the volume adsorption increased and the hysteresis loop became narrower with increasing W content in the nanofibers. The results confirmed the appearance of large amounts of finer pores in the nanofibers.²⁷ The mean pore diameters of TW0, TW10, TW20, TW30 and TW50 are 6.91, 3.62, 3.58, 3.47 and 3.24 nm, respectively, according to the calculated pore size distribution curves based on BJH theory from the desorption branch of the isotherm. The porosity of the nanofibers is beneficial to the adsorption of gas molecules.

Figure 7 shows steady state reaction rates for the gas-phase photo-oxidation of toluene by the W-doped TiO₂ nanofibers with different W contents under artificial visible light irradiation taking into account the different BET surface area of the samples. For comparison, the photocatalytic result of the commercial reference TiO₂ Degussa P25 is also showed. The reaction rates of TW0, TW10, TW20, TW30, TW50 and P25 under visible light irradiation are calculated to be of 1.02×10^{-8} , 2.59×10^{-8} , 5.12×10^{-8} , 2.98×10^{-8} , 1.98×10^{-8} , and 1.25×10^{-8} mol s⁻¹m⁻², respectively, which are much higher

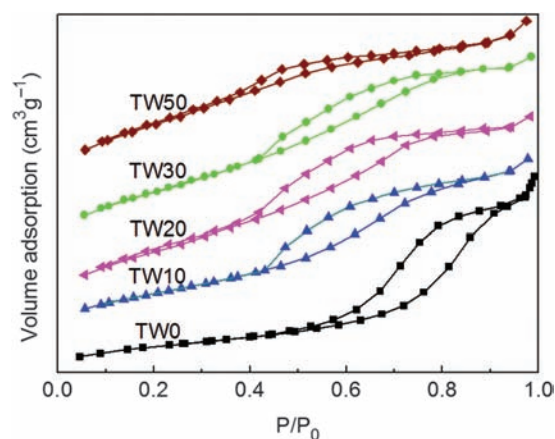


Figure 6. Nitrogen adsorption/desorption isotherm curves of TW0, TW10, TW20, TW30 and TW50.

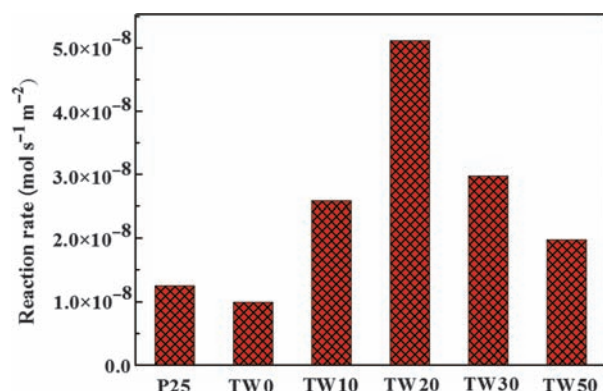
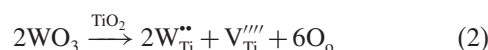
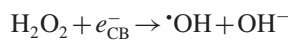
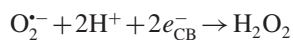
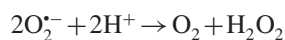
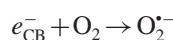
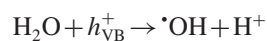
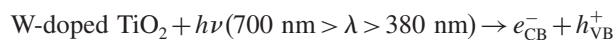


Figure 7. Toluene photo-oxidation under visible light irradiation over different photocatalysts (reaction rates, mol s⁻¹ m⁻²).

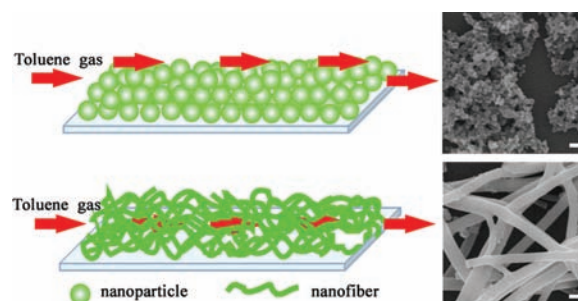
than that reported by Christoforidis' group.²⁸ W doping into TiO₂ network can be described as:



Two positive charges existed in the Ti position of anatase network after Ti⁴⁺ was replaced by W⁶⁺, along with the Ti vacancy appears. Large amounts of structural defects, both in the bulk or surface of the materials, can act as the electron capture centers, and thus increase the amounts of holes for effective photo-oxidation of toluene. The influence of W⁶⁺ in the creation of electronic states in the band gap and the concomitant decreasing of the photoabsorption band gap energy onset, increase the reaction rates of the W-doped TiO₂ nanofibers under visible light irradiation. Scheme 1 shows the energy band diagram and possible mechanism of photocatalytic reaction on W-doped TiO₂ nanofibers. The detailed photocatalytic processes are proposed as follows:



When the W-doped TiO₂ photocatalyst was radiated by visible light with a photon energy higher than or equal to the band gap between the top of the O²⁻ 2p band and the bottom of the Ti⁴⁺ 3d band, electrons (e⁻) in the 2p level of O²⁻ were excited into the conduction band of TiO₂, leaving same amount of holes (h⁺) in the 2p level of O²⁻. Holes were then captured by surface hydroxyl groups (OH⁻) on the photocatalyst surface to yield hydroxyl radicals ($\cdot\text{OH}$),²⁹ while the electrons were trapped by the



Scheme 2. Schematic diagrams of TiO₂ nanoparticles and nanofibers dispersed on the quartz tube, with the right region showing corresponding SEM images. The scale bars inserted are 100 nm.

oxygen molecules (O₂) in the air stream, producing superoxide anions (O₂^{•-}).³⁰ The similar energy of Ti 3d and W 5d levels produces widening of electronic bands (roughly similar crystal field splitting for both cations), so a narrow band gap is obtained and lower photo energy is needed to excite the photocatalyst, as shown in Scheme 1. The formed superoxide anions (O₂^{•-}) may either attack the organic molecules directly or generate hydroxyl radicals ($\cdot\text{OH}$) by reacting with hydron (H⁺) and photogenerated electrons.^{31,32} Afterward, hydroxyl radicals ($\cdot\text{OH}$), as strong oxidizing agents, degraded the organic molecules.^{33,34} Since the radii of both ions are very similar (0.061 nm for Ti⁴⁺, 0.058 nm for W⁶⁺), one does not expect large length variations in the shorter W—O bonds. However, when the W content further increased, more defects appearing in the bulk of the materials caused the distortion of the anatase TiO₂ network, as confirmed by the XRD patterns. Moreover, the defects may make a significant contribution to charge recombination, which could result in the decreasing of the reaction rates.

The nanofiber structured morphology on the quartz tube may also promote the reaction rates for the gas-phase photo-oxidation of toluene. As shown in Scheme 2, the toluene gas can pass through the loose fibers on the film, but can hardly pass through the closely packed particles. The increased contact areas between photocatalysts and toluene could greatly increase the photo-oxidation rates.

Figure 8 shows the inlet and outlet concentrations versus time for toluene and CO₂ using TW20 as the photocatalyst. The initial toluene concentration remained stable with the average value of 108.9 ppm in the whole experiment. Only small changes were found for the toluene concentration at the inlet and outlet of the quartz tube in the dark. After irradiation by the fluorescent lamp, the concentration of toluene at the outlet drastically dropped to 11.7 ppm due to the degradation of the toluene. However, the intermediate products of benzaldehyde and benzoic acid were easily formed during the toluene mineralization into CO₂ under visible light irradiation. So it is necessary to detect the CO₂ concentration to evaluate mineralization degree. As shown in Figure 8, the average CO₂ concentration before and after irradiation was about 10 ppm and

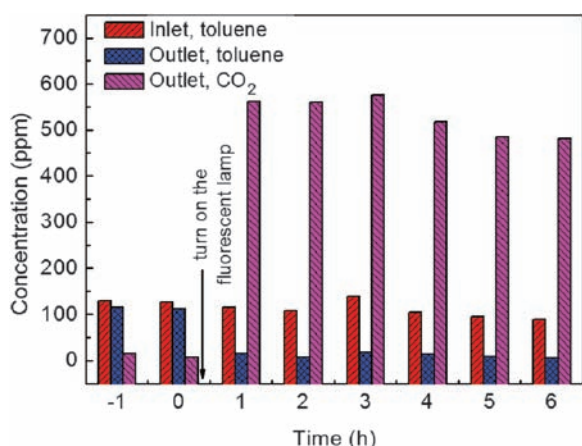


Figure 8. The inlet and outlet concentrations versus time for toluene and CO₂ using TW20 as the photocatalyst.

531.28 ppm. The mineralization degree (MD) was calculated to be 76.6% according to the following formula:

$$MD = \frac{C_{[\text{CO}_2, \text{outlet}]} - C_{[\text{CO}_2, \text{inlet}]}}{7 \times \{C_{[\text{toluene, inlet}]} - C_{[\text{toluene, outlet}]}\}} \quad (3)$$

The mineralization degree was higher than that reported in the literature,³⁵ in which nanostructured rutile TiO₂ was utilized for photocatalytic oxidation of aromatic alcohols. The mineralization degrees of TW0, TW10, TW30 and TW50 were calculated to be 20.5%, 45.8%, 58.5% and 37.4%, as listed in Table I. Moreover, the photodegradation remained stable after irradiation indicating that the catalysts were not deactivated. The higher mineralization degree can be attributed to the fiber structured morphology, the considerable visible light absorbance, high surface areas affecting adsorption of organic substrates on the surface of TiO₂ photocatalysts, as well as the OH-related surface characteristics with strong oxidizing. The surface areas increased and pores volume decreased with increasing W content in TiO₂ nanofibers as shown in Table I, indicating that more uniform pores with small diameters formed. Water molecules in the air stream with a relative humidity of 80% were adsorbed to the surface of the pores and oxidized to the ·OH radical by holes on the surface of TiO₂ under visible light irradiation. The superior oxidation ability of ·OH radical could improve the reaction rates and mineralization degree of toluene.

4. CONCLUSION

In summary, W-doped TiO₂ nanofibers with anatase structure have been prepared and samples containing up to ca. 50 wt% W mainly in substitutional positions were obtained. The crystallite size and diameter of the nanofibers decreased, while the surface areas increased, with increasing W content in the nanofibers. The W⁶⁺ in the anatase network acts as electron capture centers, which can increase the amounts of holes for effective photooxidation of toluene as well as broaden the spectral response to visible light range. Lots of uniform pores with OH-related

surface were formed in the W-doped TiO₂ nanofibers, in favor of adsorption and thorough mineralization of toluene. The sample with W content 20 wt% exhibited a degradation rate as high as $5.12 \times 10^{-8} \text{ mol s}^{-1} \text{ m}^{-2}$, 5 times higher than that of bare TiO₂ nanofibers. However, when the W content reached 50 wt% in the W-doped TiO₂ nanofibers, more defects appeared in the bulk of the material and made a significant contribution to charge recombination, which resulted in decreasing of the reaction rates.

Acknowledgments: We gratefully acknowledge the financial support by Natural Science Foundation of China (Nos. 51072034, 51172042), the Cultivation Fund of the Key Scientific and Technical Innovation Project (No. 708039), Specialized Research Fund for the Doctoral Program of Higher Education (20110075130001), Science and Technology Commission of Shanghai Municipality (12nm0503900), the Program for Professor of Special Appointment (Eastern Scholar) at Shanghai Institutions of Higher Learning, and the Program of Introducing Talents of Discipline to Universities (No. 111-2-04).

References and Notes

- B. H. Wilson, J. T. Wilson, D. H. Campbell, B. E. Bledsoe, and J. M. Armstrong, *Geomicrobiol. J.* 8, 225 (1990).
- C. L. Burnett, W. F. Bergfeld, D. V. Belsito, C. D. Klaassen, J. G. Marks, R. C. Shank, T. J. Slaga, P. W. Snyder, and F. A. Andersen, *Int. J. Toxicol.* 29, 61S (2010).
- R. Font, M. C. Sabater, and M. A. Martínez, *Environ. Sci. Technol.* 35, 977 (2001).
- V. Augugliaro, S. Coluccia, V. Lodo, L. Marchese, G. Martra, L. Palmisano, and M. Schiavello, *Appl. Catal. B: Environ.* 20, 15 (1999).
- M. Jin, X. T. Zhang, H. T. Pu, S. Nishimoto, T. Murakami, and A. Fujishima, *J. Colloid Interf. Sci.* 362, 188 (2011).
- Y. J. Tham, P. A. Latif, A. M. Abdullah, A. Shamala-Devi, and Y. H. Taufiq-Yap, *Bioresour. Technol.* 102, 724 (2011).
- A. Fujishima and X. T. Zhang, *C. R. Chim.* 9, 750 (2006).
- J. H. Mo, Y. P. Zhang, Q. J. Xu, J. J. Lamson, and R. Y. Zhao, *Atmos. Environ.* 43, 2229 (2009).
- M. R. Hoffmann, S. T. Martin, W. Y. Choi, and D. W. Bahnemann, *Chem. Rev.* 95, 69 (1995).
- R. Asahi, T. Morikawa, T. Ohwaki, K. Aoki, and Y. Taga, *Science* 293, 269 (2001).
- H. Y. Xie, Y. N. Zhang, and Q. L. Xu, *J. Nanosci. Nanotechnol.* 10, 5445 (2010).
- A. Fuerte, M. D. Hernández-Alonso, A. J. Maira, A. Martínez-Arias, M. Fernández-García, J. C. Conesa, and J. Soria, *Chem. Commun.* 37, 2718 (2001).
- A. Fuerte, M. D. Hernández-Alonso, A. Iglesias-Juez, A. Martínez-Arias, J. C. Conesa, J. Soria, and M. Fernández-García, *Phys. Chem. Chem. Phys.* 5, 2913 (2003).
- D. Li and Y. N. Xia, *Adv. Mater.* 16, 1151 (2004).
- X. M. Sui, C. L. Shao, and Y. C. Liu, *Polymer* 48, 1459 (2007).
- D. Li and Y. N. Xia, *Nano Lett.* 3, 555 (2003).
- X. F. Lu, X. C. Liu, W. J. Zhang, C. Wang, and Y. Wei, *J. Colloid Interf. Sci.* 298, 996 (2006).
- N. Coucelo, F. S. G. Einschlag, R. J. Candal, and M. Jobbagy, *J. Phys. Chem. C* 112, 1094 (2008).
- L. Zhang, Y. G. Li, Q. H. Zhang, G. Y. Shi, and H. Z. Wang, *Chem. Lett.* 40, 1371 (2011).

20. T. Okumura, Y. Kinoshita, H. Uchiyama, and H. Imai, *Mater. Chem. Phys.* 111, 486 (2008).
21. R. D. Shannon and C. T. Prewitt, *Acta Crystallogr. B* 25, 925 (1969).
22. C. H. Wang, C. L. Shao, X. T. Zhang, and Y. C. Liu, *Inorg. Chem.* 48, 7261 (2009).
23. M. Penza, M. A. Tagliente, L. Mirengi, C. Gerardi, C. Martucci, and G. Cassano, *Sensor. Actuat. B: Chem.* 50, 9 (1998).
24. Y. P. He, Z. Y. Wu, L. M. Fu, C. R. Li, Y. M. Miao, L. Cao, H. M. Fan, and B. S. Zou, *Chem. Mater.* 15, 4039 (2003).
25. J. K. Burdett, T. Hughbanks, G. J. Miller, J. W. Richardson, and J. V. Smith, *J. Am. Chem. Soc.* 109, 3639 (1987).
26. B. Smarsly, S. Polarz, and M. Antonietti, *J. Phys. Chem. B* 10, 10473 (2001).
27. K. S. W. Sing, D. H. Everett, R. A. W. Haul, L. Moscou, R. A. Pierotti, J. Rouquerol, and T. Siemieniewska, *Pure Appl. Chem.* 57, 603 (1985).
28. K. C. Christoforidis, S. J. A. Figueroa, and M. Fernández-García, *Appl. Catal. B: Environ.* 117, 310 (2012).
29. N. Zhang, S. Q. Liu, X. Z. Fu, and Y. J. Xu, *J. Phys. Chem. C* 115, 9136 (2011).
30. J. Yang, C. C. Chen, H. W. Ji, W. H. Ma, and J. C. Zhao, *J. Phys. Chem. B* 109, 21900 (2005).
31. L. R. Zheng, Y. H. Zheng, C. Q. Chen, Y. Y. Zhan, X. Y. Lin, Q. Zheng, K. M. Wei, and J. F. Zhu, *Inorg. Chem.* 48, 1819 (2009).
32. H. C. Yatmaz, A. Akyol, and M. Bayramoglu, *Ind. Eng. Chem. Res.* 43, 6035 (2004).
33. O. Legrini, E. Oliveros, and A. M. Braun, *Chem. Rev.* 93, 671 (1993).
34. J. Xu, W. Z. Wang, M. Shang, E. P. Gao, Z. J. Zhang, and J. Ren, *J. Hazard. Mater.* 196, 426 (2011).
35. S. Yurdakal, G. Palmisano, V. Loddo, V. Augugliaro, and L. Palmisano, *J. Am. Chem. Soc.* 130, 1568 (2008).

Received: 23 September 2013. Accepted: 12 January 2014.

Delivered by Publishing Technology to: University of New South Wales
IP: 206.214.8.126 On: Mon, 11 Apr 2016 04:06:16
Copyright: American Scientific Publishers